


Electron-phonon coupling, thermal expansion coefficient, resonance effect, and phonon dynamics in high-quality CVD-grown monolayer and bilayer MoSe₂

Deepu Kumar^{1,*}, Vivek Kumar,¹ Rahul Kumar², Mahesh Kumar², and Pradeep Kumar^{1,†}

¹*School of Basic Sciences, Indian Institute of Technology Mandi, Mandi-175005, India*

²*Department of Electrical Engineering, Indian Institute of Technology Jodhpur, Jodhpur-342037, India*

 (Received 1 August 2021; revised 5 February 2022; accepted 7 February 2022; published 22 February 2022)

Probing phonons, quasiparticle excitations, and their coupling has enriched our understanding of two-dimensional (2D) materials and proved to be crucial for developing their potential applications. Here, we report comprehensive temperature 4–330 K and polarization-dependent Raman measurements on monolayer (1L) and bilayer (2L) MoSe₂. Phonon modes up to the fourth order are observed, including forbidden Raman and infrared modes, and understood considering the Fröhlich mechanism of exciton-phonon coupling. Most notably, anomalous variations in the phonon linewidths with temperature point at the significant role of electron-phonon coupling in these systems, especially for the out-of-plane (A_{1g}) and shear modes (E_{2g}^2), which is found to be more prominent in the narrow-gapped 2L than the large gapped 1L. We deciphered the ambiguity in symmetry assignments, especially to the peaks ~ 170 and ~ 350 cm⁻¹ via polarization-dependent measurements. Temperature-dependent thermal expansion coefficient, an important parameter for device performance, is carefully extracted for both 1L and 2L by monitoring the temperature dependence of the real part of the phonon self-energy parameter. Our temperature-dependent in-depth Raman studies pave a way for uncovering the deeper role of phonons in these 2D layered materials from a fundamental as well as application point of view.

DOI: [10.1103/PhysRevB.105.085419](https://doi.org/10.1103/PhysRevB.105.085419)

I. INTRODUCTION

Group-VI transition metal dichalcogenides (TMDCs) in their naturally obtained bulk form have been studied for decades due to their rich physics and industrial applications [1,2]. These TMDC materials have gained much research attention after the successful isolation of single-layer graphene from graphite [3]. These are the layered materials belonging to the family of two-dimensional (2D) materials with a common atomic formula MX_2 , where M is the transition-metal atom (Mo or W), and X is the chalcogen atom (S, Se, or Te) [4–8]. TMDCs with monolayer (1L) thickness have attracted considerable attention due to their unique electronic, optoelectronic, spin, and valley properties, making them promising materials for the future high-performance devices [6,9,10].

MoSe₂ is one of the crucial members of the TMDC family with small direct bandgap, high carrier mobility, and on-off ratio $> 10^6$ [4,6]. Bulk (1L) MoSe₂ shows an indirect (direct) bandgap with a value of 1.1 eV (1.54 eV) [11]. The performance of electronic and optical devices based on the MoSe₂ and other 2D materials will be significantly influenced by the change of thermal properties such as their thermal expansion coefficient (TEC) and thermal conductivity with temperature. Generally, 2D materials are supported by some substrates, like SiO₂/Si for device applications, which induce strain into the system due to the TEC mismatch between

MX_2 and the substrate, and it significantly impacts the fundamental properties of these 2D materials [12,13]. Therefore, to increase the performance and reliability of electronic and optical devices based on these TMDCs, it becomes pertinent to understand the behavior of TEC as a function of temperature and induced strain or stress due to the TEC mismatch between MX_2 and the substrate. The Raman spectroscopic technique has proved to be very useful for probing 2D as well as bulk systems and their various aspects such as layer stacking geometry, strain effect, thermal properties, defects, and number of layers [5,7,12–20]. Several authors have employed temperature-dependent Raman scattering to estimate thermal properties like TEC and thermal conductivity by monitoring the behavior of the phonon modes as a function of temperature [14–16]. Additionally, anharmonicity present in the material affects the dynamics of the charge carriers by controlling the strength of electron-phonon and phonon-phonon interactions, which may also significantly impact the functioning of the device. Electron-phonon coupling in 2D materials plays a crucial role in controlling ballistic transport and dynamics of an excited state. Anharmonicity, resulting from phonon-phonon interactions and electron-phonon coupling, may be understood by monitoring the temperature-dependent behavior of the phonon modes.

Here, we report an in-depth temperature-dependent Raman study on layered MoSe₂, grown by the chemical vapor deposition (CVD) method, in a wide temperature range of 4 to 330 K. The measurements were done on both 1L and bilayer (2L) MoSe₂. We extracted the TEC by monitoring the temperature dependence of the first-order optical phonon modes. We have also focused on the temperature-dependent behavior

*deepu7727@gmail.com

†pkumar@iitmandi.ac.in

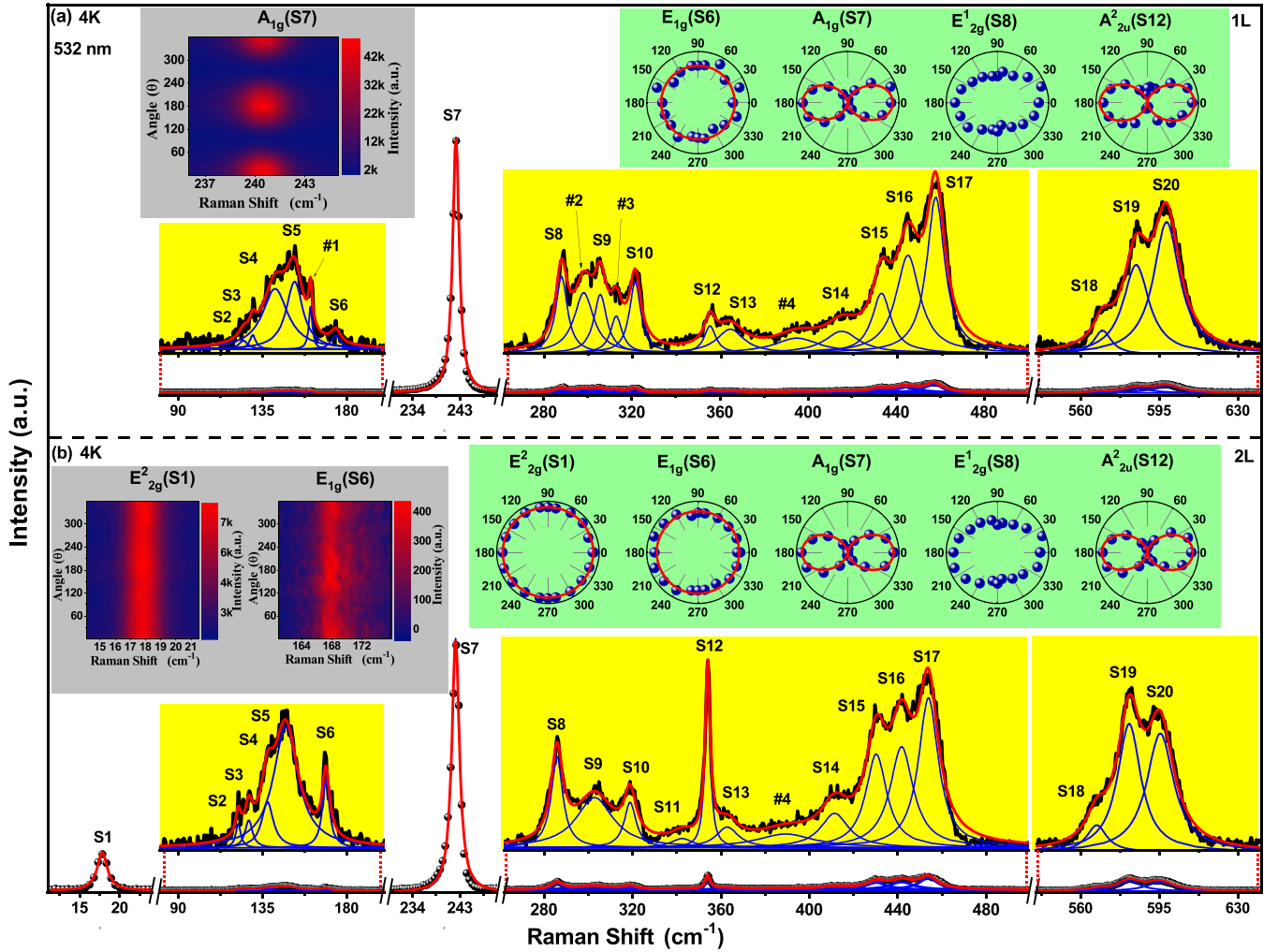


FIG. 1. Raman spectra of (a) monolayer (1L) and (b) bilayer (2L) MoSe₂ at 4 K. Insets in the yellow shaded area show the amplified spectra. Insets in the green shaded area show the intensity polar plot of the E_{2g}^2 , E_{1g} , A_{1g} , E_{2g}^1 , and A_{2u}^2 modes; solid red lines are the fitted curves as described in the text. Insets in gray area illustrate the two-dimensional (2D) color contour maps of the Raman intensity vs Raman shift and as a function of the polarization angle for 1L and 2L MoSe₂.

of the low-frequency interlayer modes, forbidden Raman- or infrared (IR)-active modes, and especially the second- and higher-order phonon modes. Interestingly, we observed the broadening of the A_{1g} and E_{2g}^2 shear phonon modes in the low-temperature window attributed to the electron-phonon coupling. We believe that our detailed studies will pave the way for further studies on MoSe₂ and other 2D materials in this direction.

II. RESULTS AND DISCUSSIONS

A. Multiphonon Raman scattering in MoSe₂

Details about the synthesis, Raman, and photoluminescence (PL) measurements are given in the Secs. 1–3 in the Supplemental Material [21]. We used Raman and PL to identify the number of layers of the flakes, as has also been done in the previous reports on TMDC systems [7, 19, 22, 23], and thickness of the flakes is determined using atomic force microscopy (AFM), see the Supplemental Material [21] for more details. Figures 1(a) and 1(b) show the Raman spectrum of 1L and 2L MoSe₂ at 4 K, in a spectral range of 10–640 cm⁻¹,

respectively. In the yellow shaded area, insets show the amplified spectra in the spectral range of 80–200, 260–500, and 540–640 cm⁻¹. The spectra are fitted with a sum of Lorentzian functions to extract mode frequency (ω), full width at half maximum (FWHM), and intensity of the individual mode. For convenience, we have labeled the observed modes as S1–S20, which along with their corresponding symmetries are listed in Table I. For details about the phonon modes at the Γ point, see Supplemental Material Secs. 2–3 [21]. The symmetry assignment of the modes is done according to the previous reports and our polarization-dependent measurements. The observed modes are in excellent agreement with the recently published reports on high-quality MoSe₂ samples grown by vapor phase chalcogenization and the mechanical exfoliation method [19, 24]. However, the observed modes in our case using 532 nm laser excitation are relatively weak compared with the observed modes with excitation energies in the range of 2.41–2.81 eV [25]. The E_{2g}^2 (S1) mode is observed at 17.4 cm⁻¹ for 2L (absent for 1L). A_{1g} (S7) and E_{2g}^1 (S8) are observed at 242.3, 242.2 cm⁻¹ and 287.9, 285.9 cm⁻¹ in 1L and 2L, respectively. Observed Raman modes \sim 170 and

TABLE I. List of the experimentally observed modes along with their symmetry assignments and frequency at 4 K for the 1L and 2L MoSe₂. Units are in cm⁻¹.

Mode assignment	Frequency (ω)	
	1L	2L
S1 [$E_{2g}^2(\Gamma)$]	–	17.8 ± 0.02
S2 [TA($M-K$)]	124.8 ± 0.8	121.9 ± 0.3
S3 [ZA($M-K$)]	129.7 ± 0.5	127.6 ± 0.4
S4 [$E_{2g}^1 - LA(M)$]	140.7 ± 0.8	137.8 ± 0.3
S5 [LA(M)]	152.1 ± 0.3	147.3 ± 0.3
#1	160 ± 1.0	–
S6 [$E_{1g}(\Gamma)$]	174.1 ± 0.6	168.8 ± 0.4
S7 [$A_{1g}(\Gamma)$]	242.3 ± 0.1	242.2 ± 0.02
S8 [$E_{2g}^1(\Gamma)$]	287.9 ± 0.2	285.9 ± 0.2
#2	298.0 ± 0.5	–
S9 [2LA(M)]	305.5 ± 0.3	302.8 ± 0.4
#3	312.7 ± 0.8	–
S10	321.2 ± 0.1	318.9 ± 0.2
S11	–	342.5 ± 0.5
S12 [$A_{2u}^2(\Gamma)$]	355.1 ± 0.4	354.0 ± 0.03
S13 [$A_{1g}(M) + LA(M)$]	364.3 ± 1.0	362.8 ± 0.7
#4	387.4 ± 2.5	389.2 ± 2.5
S14 [TA(M) + 2LA(M)]	414.6 ± 1.2	411.4 ± 0.6
S15 [$E_{2g}^1(M) + LA(M)$]	432.7 ± 0.3	430.2 ± 0.2
S16 [$A_{2u}^2(M) + LA(M)$]	444.6 ± 0.2	441.7 ± 0.3
S17 [3LA(M)]	457.2 ± 0.1	453.9 ± 0.1
S18 [TA(M) + 3LA(M)]	569.7 ± 0.4	567.0 ± 0.4
S19 [$E_{2g}^1(M) + 2LA(M)$]	584.6 ± 0.2	581.6 ± 0.1
S20 [4LA(M)]	598.2 ± 0.1	595.4 ± 0.4

~352 cm⁻¹ have been assigned as E_{1g} and A_{2u}^2 modes, respectively, in earlier studies [19]. However, the peak observed ~352 cm⁻¹ is also assigned as B_{2g}^1/A_{2u} [23,26], suggesting some ambiguity in assigning proper symmetry to this mode. E_{1g} mode is Raman active but is normally forbidden in backscattering Raman measurements, while the A_{2u}^2 mode is IR active and is associated with the out-of-plane vibration of both the Mo and Se atoms, see inset in Fig. S1(e) in the Supplemental Material [21]. E_{1g} (S6) and A_{2u}^2 (S12) are observed at 174.1, 168.8 cm⁻¹ and 355.1, 354 cm⁻¹ in 1L and 2L, respectively.

In addition to the well-known first-order optical modes, E_{2g}^2 , E_{1g} , A_{1g} , E_{2g}^1 , and A_{2u}^2 , we also observe first-order longitudinal acoustic (LA), transverse (TA), and out-of-plane (ZA) modes near M or K symmetry points in the Brillouin zone (BZ) along with a large number of second- or higher-order phonon modes. The first-order LA mode near the M point of the BZ is observed at 152.1 and 147.3 cm⁻¹ in 1L and 2L MoSe₂, respectively. Toward the low-frequency side of the LA(M) (S5) mode, two weak modes S2 and S3 are observed at 124.8 (129.7) and 121.9 (127.6) cm⁻¹ in 1L (2L) and are assigned as TA and ZA, respectively, along the $M-K$ direction in the BZ [19]. In the case of the 1L, overtones and combinations of optical and acoustical phonon modes from the M symmetry point of the BZ are observed at 140.7 cm⁻¹ [$E_{2g}^1 - LA(M)$; S4], 305.5 cm⁻¹ [2LA(M); S9], 364.3 cm⁻¹ [$A_{1g}(M) + LA(M)$; S13], 414.6 cm⁻¹ [TA(M) + 2LA(M); S14],

432.7 cm⁻¹ [$E_{2g}^1(M) + LA(M)$; S15], 457.2 cm⁻¹ [3LA(M); S17], 569.7 cm⁻¹ [TA(M)+3LA(M); S18], 584.6 cm⁻¹ [$E_{2g}^1(M) + 2LA(M)$; S19], and at 598.2 cm⁻¹ [4LA(M); S20]. In the case of the 2L, the observed second- and higher-order phonon modes and their corresponding symmetry assignment are given in Table I. Further, we notice a mode S16 at ~444.6 (441.7) cm⁻¹ in 1L (2L) at 4 K, while at room temperature, this mode is observed at ~441.5 (339.1) cm⁻¹ in 1L (2L) MoSe₂. The energy of this mode is close to the sum of A_{2u}^2 (S12) and LA (S5) modes from M point of the BZ. Interestingly, this mode is absent when the spectra are excited using a 632.8 nm laser, see inset in Fig. S2(b) in the Supplemental Material [21]. The appearance of these forbidden and IR-active phonons modes from the BZ center and multiphonon Raman scattering from other parts of the BZ may be understood via resonance effect [23,27], Fröhlich mechanism of exciton-phonon coupling [28], and cascade theory of inelastic light scattering [29], see Sec. 6 in the Supplemental Material [21] for detailed discussion on the origin of these modes.

To decipher the symmetry assignment and to understand the angle-dependent nature of the phonon modes with respect to the polarization direction of the incident photon, especially for E_{1g} (S6) and A_{2u}^2 (S12) modes ~170 and 350 cm⁻¹, respectively, we carried out a detailed polarized Raman scattering measurements for both 1L and 2L of MoSe₂. The polarization-dependent measurements were done by rotating the direction of the incident light at an angle (θ) by keeping the position of the sample and direction of the scattered light fixed, as described in Refs. [30,31]. Insets in the green shaded area, see Figs. 1(a) and 1(b), are the angular dependence of the intensity polar plots of the modes E_{2g}^2 (S1), E_{1g} (S6), A_{1g} (S7), E_{2g}^1 (S8), and A_{2u}^2 (S12) for both 1L and 2L. The intensity of the E_{2g}^2 (S1) mode shows isotropic nature with respect to the polarization angle, i.e., intensity is invariant with respect to the rotation of polarization angle. However, the intensity of the A_{1g} mode shows a twofold symmetric nature, i.e., it has a maximum intensity at both 0° and 180°, while the intensity approaches zero at 90° and 270°. The angular dependence of the intensity of the mode E_{1g} (S6) is like the E_{2g}^2 mode. The polarization-dependent results discussed above could also be seen in the 2D color contour maps of the Raman intensity vs Raman shift and as a function of polarization angle, which are shown as insets for (a) A_{1g} and (b) E_{2g}^2 and E_{1g} in Fig. 1 in the gray area for 1L and 2L MoSe₂, respectively. Intensity of the E_{2g}^1 (S8) mode showed dependence on the rotation angle against the expected isotropic behavior; its intensity is more at 0° than at 90°, while angular dependence of the intensity of the mode A_{2u}^2 (S12) is like that of the A_{1g} mode. Based on our polarization-dependent Raman observations and IR measurements from literature [2], we attribute modes ~170 (S6) and ~350 cm⁻¹ (S12) to the first-order Raman-active E_{1g} mode and IR-active A_{2u}^2 mode, respectively.

The observed variation in intensity as a function of polarization angle may be understood within a semiclassical approximation. As the incident and scattered polarized light lie in the xy plane, the unit vector associated with incident (\hat{e}_i) and scattered (\hat{e}_s) light of polarization may be decomposed as $[\cos(\theta + \theta_0), \sin(\theta + \theta_0), 0]$ and $[\cos(\theta_0), \sin(\theta_0), 0]$, respectively, where θ_0 is an arbitrary angle from the x axis, and

θ varies from 0° to 360° . Within the semiclassical approximation, Raman scattering intensity of the first-order phonon modes is given as $I_{\text{int}} = |\hat{\epsilon}'_s R \hat{\epsilon}_i|^2$, where R is the Raman tensor [32,33]. Using the above expression and Raman tensor [33], the intensities of the E_{1g} , A_{1g} , and E_{2g}^1 modes for our experimental geometry are given as $I_{E_{1g}} = 0$, $I_{A_{1g}} = a \cos^2\theta$, and $I_{E_{2g}^1} = d^2(\cos^2\theta + \sin^2\theta)$, respectively. Within the semiclassical approximation, the following observations can be made: (i) Intensity of the E_{1g} mode is zero, suggesting it should be absent in the backscattering geometry. (ii) Intensity of the A_{1g} mode is maximum when $\hat{\epsilon}_i$ and $\hat{\epsilon}_s$ are parallel to each other, i.e., $\theta = 0^\circ$, and it reduces to zero when $\theta = 90^\circ$. (iii) Intensity of the E_{2g}^1 mode remains invariant with respect to the rotation of polarization angle. From our above discussions, we may conclude that, within the semiclassical approximation, the modes with E -type symmetry are not affected by polarization configuration and are either observed or forbidden in both parallel and cross-polarization configuration. However, modes with A -type symmetry are strongly affected by the polarization configuration and can be observed only in parallel configuration. The solid lines are the fitted curves from the above expressions, suggesting that the experimental results are in very good agreement with the semiclassical approximation. The intensity pattern of the E_{2g}^1 mode in both 1L and 2L MoSe₂ is slightly smaller in cross-configuration than the parallel configuration and forms a semilobe kind of structure [see Figs. 1(a) and 1(b)]. The observed deviation of the E_{2g}^1 mode intensity from the predicted one may arise due to the electron-photon-phonon coupling, which may be understood within the quantum mechanical picture [31]. We also did polarization-dependent measurements on the additional 1L and 2L flakes of those shown in Fig. S3 in the Supplemental Material [21]. Intensity polar plots of the modes E_{2g}^2 (S1), E_{1g} (S6), A_{1g} (S7), E_{2g}^1 (S8), and A_{2u}^2 (S12) are shown in Fig. S5 in the Supplemental Material [21] and are found to be like those shown in Fig. 1.

B. TEC and temperature-dependent frequency of the first-order optical modes

To understand the temperature dependence of the phonon modes quantitatively, we plotted the self-energy parameters such as mode frequency (ω) and FWHM (Γ) of the phonon modes as a function of temperature. Figure 2(a) illustrates temperature dependence of the frequency of the A_{1g} (S7) and E_{2g}^1 (S8) phonon modes for 1L MoSe₂. Both these modes, i.e., A_{1g} and E_{2g}^1 , stiffen with the decreasing temperature down to ~ 80 K, and below this, a slight rise (drop) in frequency is observed for the case of A_{1g} (E_{2g}^1). On further cooling, until 4 K, both these modes remain nearly temperature independent. Figure 2(b) illustrates temperature dependence of the frequency of A_{1g} and E_{2g}^1 phonon modes for 2L MoSe₂. Both A_{1g} and E_{2g}^1 modes stiffen with the decreasing temperature down to ~ 80 K; interestingly, a softening in frequency is observed for both the phonon modes on further cooling. Figure 3(a) shows the temperature dependence of the frequency forbidden E_{1g} (S6) mode for 1L. We observed that variations in the frequency of E_{1g} in the temperature window 330 to ~ 80 K is normal, and at ~ 80 K, a drop in frequency is observed for

the case of the E_{1g} mode, and < 80 K, it again starts to harden on further cooling until 4 K. Figure 3(b) shows the temperature dependence of the frequency of the E_{2g}^2 (S1), E_{1g} (S6), and A_{2u}^2 (S12) modes for 2L. Temperature-dependent behavior of the mode A_{2u}^2 is like that of A_{1g} and E_{2g}^1 modes for 2L [see Fig. 2(b)]. The temperature-dependent shift in the frequency of the E_{2g}^2 and E_{1g} modes is interesting, probably arising from the temperature effect on the interlayer strength. The temperature dependence of these forbidden and IR-active modes needs further theoretical understanding. Details about the temperature dependence of the first-order acoustic, second-, and higher-order phonon modes are given in the Supplemental Material Sec. 7 [21].

The temperature-dependent shift in frequency of the phonon modes of the freestanding MoSe₂ may be understood via (i) anharmonic effect, which arises due to change in the self-energy parameter because of phonon-phonon coupling, or (ii) quasi-harmonic effect, which arises due to thermal expansion of the lattice. The change in the phonon mode frequency as a function of temperature considering the above two effects may be given as

$$\Delta\omega(T) = \Delta\omega_{\text{Anh}}(T) + \Delta\omega_E(T). \quad (1)$$

The first term in Eq. (1) arises due to a change in phonon self-energy because of the anharmonic effect and is given as [34] $\Delta\omega_{\text{Anh}}(T) = \omega_{\text{Anh}}(T) - \omega_0 = D(1 + \frac{2}{e^x - 1})$, where $x = \hbar\omega/2k_B T$, and D is a self-energy constant parameter, representing the contributions from the three-phonon anharmonic effect. In the simplest Klemens model, considering only the three-phonon process, an optical phonon is assumed to decay into two phonons with equal frequency and opposite momentum. Furthermore, with the variations in temperature, the lattice parameter of the MoSe₂ would change due to thermal expansion, resulting in a variation in the phonon mode frequency as a function of temperature. The contribution of thermal expansion effect to the shift in phonon mode frequency is given as [35] $\Delta\omega_E(T) = \omega_E(T) - \omega_0 = \omega_0 \exp[-3\gamma \int_{T_0}^T \alpha_{\text{MoSe}_2}(T) dT] - \omega_0$, where γ is the Gruneisen parameter of a particular mode and $\alpha_{\text{MoSe}_2}(T)$ is the temperature-dependent TEC of MoSe₂. We note that both positive and negative TEC have been reported for MoSe₂ [36–38]. In the present case, MoSe₂ is not freestanding but is supported by the SiO₂/Si substrate, and SiO₂ has a negative (positive) TEC at low (high) temperature [39]. Therefore, in addition to the abovementioned two effects (i.e., anharmonic and thermal expansion effects), thermally induced strain results from TEC mismatch between MoSe₂ and substrate should also be considered to understand the net change in the phonon mode frequency with temperature. Change in the phonon mode frequency, considering these effects, as a function of temperature is given as [15,34,35]

$$\omega(T) = \omega_0 + \Delta\omega_{\text{Anh}}(T) + \Delta\omega_E(T) + \Delta\omega_S(T). \quad (2)$$

The last term $\Delta\omega_S(T)$ is the change in the mode frequency corresponding to the strain effect due to the TEC mismatch. It can be expressed as [15] $\Delta\omega_S(T) = \omega_S(T) - \omega_0 = \beta\epsilon(T) = \beta \int_{T_0}^T [\alpha_{\text{SiO}_2}(T) - \alpha_{\text{MoSe}_2}(T)] dT$, where ϵ is the induced strain due to the TEC mismatch between the MoSe₂ film and the substrate, β is the strain coefficient of a particular mode,

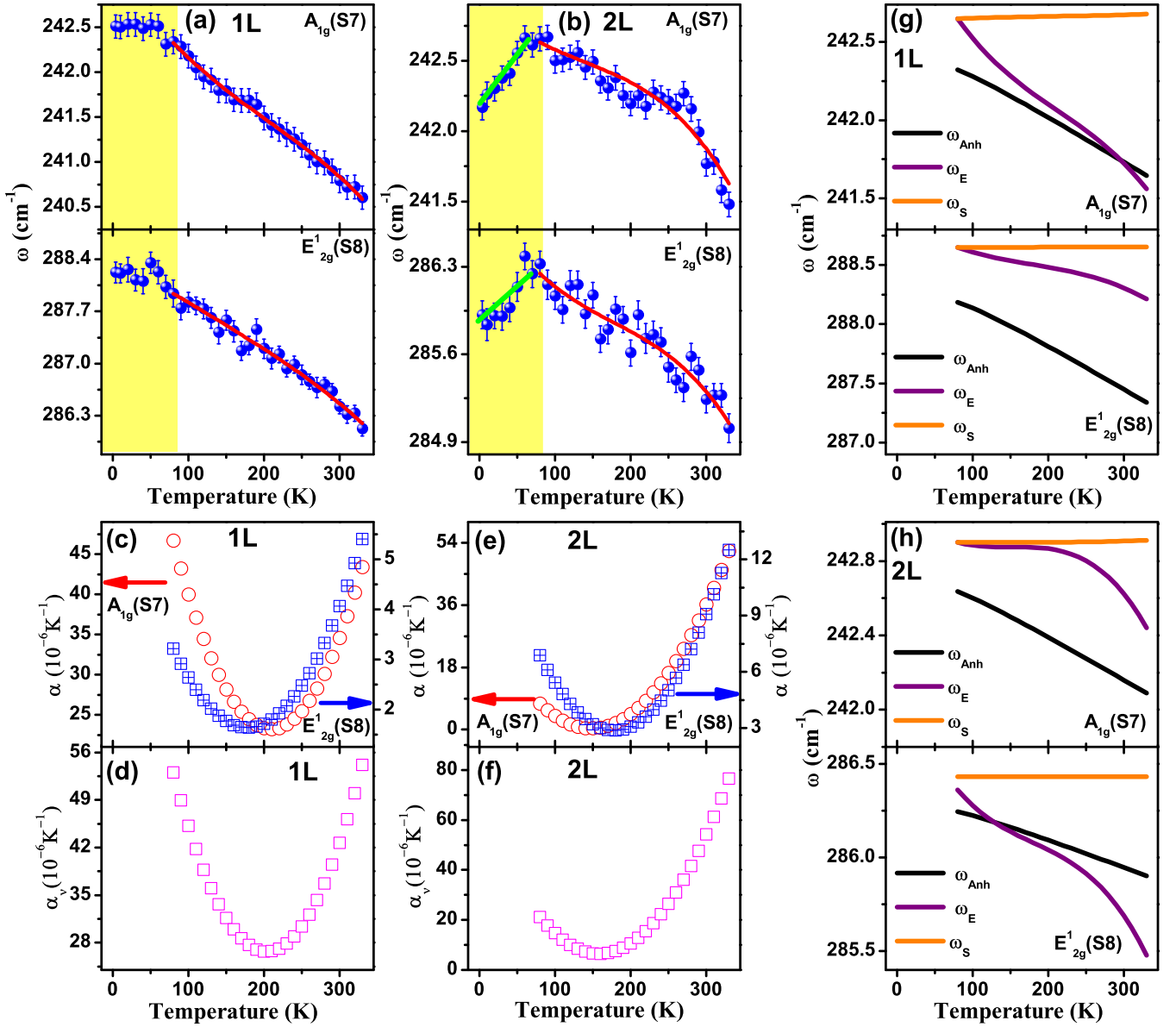


FIG. 2. (a) and (b) Temperature dependence of the frequency of A_{1g} and E_{2g}^1 modes for monolayer (1L) and bilayer (2L) MoSe₂, respectively. The error bars for frequencies are extracted using Lorentzian fitting. Solid red lines are the fitted curves as described in the text, and the solid green lines are a guide to the eye. The shaded part illustrates the region where the mode frequency shows anomalous behavior. (c) and (e) Linear thermal expansion coefficient (TEC) corresponding to the A_{1g} (red) and E_{2g}^1 (blue) modes. (d) and (f) Volumetric TEC in the temperature range of 80–330 K for 1L and 2L MoSe₂, respectively. (g) and (h) Individual contributions to the frequency from three-phonon anharmonic effect (black), thermal expansion effect (purple), and strain effect due to TEC mismatch (orange) for 1L and 2L, respectively.

and $\alpha_{\text{SiO}_2}(T)$ is the temperature-dependent TEC of SiO₂. To estimate $\alpha_{\text{MoSe}_2}(T)$, we have used the value of $(\beta = \frac{\partial\omega}{\partial\varepsilon})$ as $\beta_{A_{1g}} = -3.7 \text{ cm}^{-1}/\%$ and $\beta_{E_{2g}^1} = -1.2 \text{ cm}^{-1}/\%$ [12]. The TEC of SiO₂ was taken from Ref. [39] and was integrated out while estimating TEC for MoSe₂. The product of the mode Grüneisen parameter and the TEC may be expressed by a polynomial of temperature and is given as

$$\gamma\alpha_{\text{MoSe}_2}(T) = p_0 + p_1T + p_2T^2, \quad (3)$$

where p_0 , p_1 , and p_2 are the constant parameters, whose values are obtained as a fitting parameter by the best fit to

the temperature dependence of the frequency of the modes. To extract the TEC of MoSe₂, we have fitted the frequency of A_{1g} and E_{2g}^1 modes in the temperature range of 80–330 K for 1L and 2L using the Eqs. (2) and (3). The above Eq. (3) can be used to estimate the TEC as a function of temperature. Since there are no experimental values available in the literature for the mode Grüneisen parameter for MoSe₂, we have adopted the average value of the Grüneisen parameter (~ 0.2 for A_{1g} and ~ 0.8 for E_{2g}^1 modes) for 2D TMDCs to estimate the TEC of MoSe₂ in both out-of-plane and in-plane directions [40].

Figures 2(c) and 2(e) show the temperature-dependent TEC of the in-plane (E_{2g}^1) and out-of-plane (A_{1g}) modes for

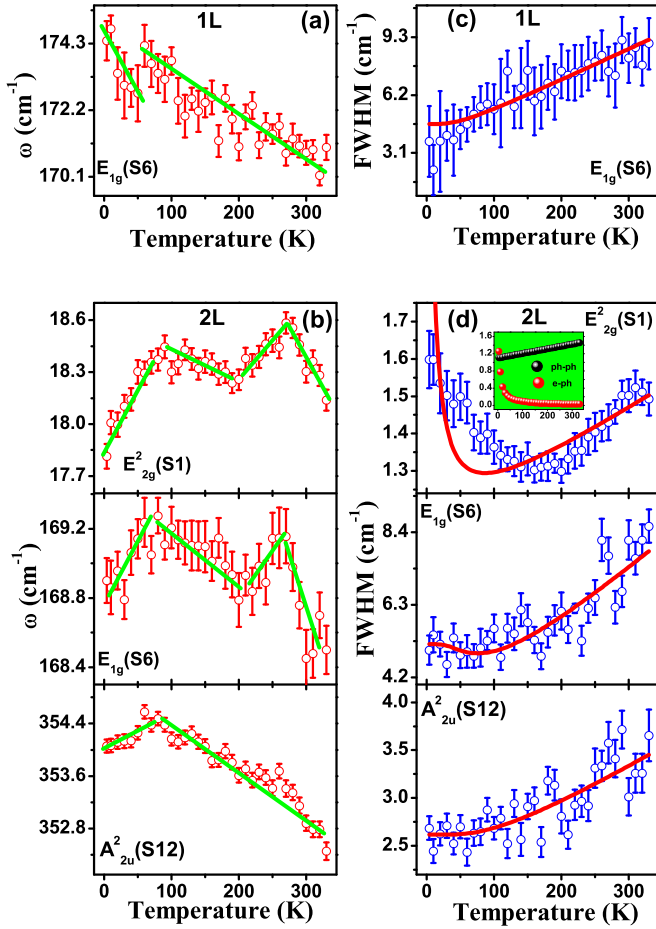


FIG. 3. Temperature-dependent (a) frequency and (c) full width at half maximum (FWHM) of the E_{1g} mode for the monolayer (1L). Temperature-dependent (b) frequency and (d) FWHM of E_{2g}^2 , E_{1g} , and A_{2u}^2 modes for the bilayer (2L). Solid red lines are the fitted curves described in the text, and solid green lines are a guide to the eye. Inset black and red plots in (d) describe individual contributions to the linewidth from phonon-phonon and electron-phonon coupling, respectively.

1L and 2L MoSe₂ in a temperature range of 80 to 330 K, respectively. Our temperature-dependent results show that the TEC of the A_{1g} mode for both systems (1L and 2L MoSe₂) decreases with decreasing temperature starting from 330 to \sim 200 K; on further cooling, an increase in TEC is observed for 1L and 2L. While the TEC corresponding to the E_{2g}^1 mode decreases with decreasing temperature from 330 to \sim 200 K, surprisingly, <180 K, an increase is seen on further lowering the temperature. We also estimated the volumetric TEC given as $\alpha_v = 2\alpha_a + \alpha_c$ [37], where α_a and α_c are the linear TEC for in-plane and out-of-plane directions. Figures 2(d) and 2(f) show the volumetric TEC as a function of temperature. Room temperature linear TEC corresponding to the E_{2g}^1 and A_{1g} modes, together with volumetric TEC, is listed in Table II. The volumetric TEC values at room temperature are found to be 42.7×10^{-6} and $54.3 \times 10^{-6} \text{ K}^{-1}$ for 1L and 2L MoSe₂, respectively (see Table II). The estimated volumetric TEC results are \sim 2–3 times larger than that of the reported value for 1L MoSe₂ supported by SiO₂/Si substrate [41]. Our estimated

TABLE II. Room temperature linear and volumetric TEC for 1L and 2L MoSe₂ extracted using E_{2g}^1 and A_{1g} modes. Units are in 10^{-6} K^{-1} .

MoSe ₂	$\alpha(E_{2g}^1)$	$\alpha(A_{1g})$	$\alpha_v = 2\alpha_a + \alpha_c$
1L	4.1	34.5	42.7
2L	9.1	36.1	54.3

linear in-plane TEC value for the 1L is very close to the theoretically calculated TEC for 1L MoSe₂ [38], while it is nearly 10 times smaller than that of experimentally reported in-plane TEC for freestanding 1L MoSe₂ [42]. Furthermore, the TEC corresponding to the A_{1g} mode is larger than that of the E_{2g}^1 mode for 1L, which is in line with earlier reports on other TMDCs [43,44]. The larger TEC of the A_{1g} mode may be understood as, in layered materials, the out-of-plane direction is confined weakly compared with the in-plane direction; therefore, it is easier to deform the out-of-plane direction than the in-plane direction [45]. For 2L, an increment in TEC of the E_{2g}^1 mode is observed compared with that of the 1L, which differs from the earlier report on MoSe₂ [42].

Now we will focus on the observed anomalies in the mode frequencies at low temperature. The observed kink in frequencies of the modes at low temperature for 1L, as shown in Figs. 2(a) and 3(a), may be due to induced strain owing to TEC mismatch between MoSe₂ and the substrate. The induced strain due to the TEC mismatch may affect the weak van der Waals forces, leading to the slippage, realignment, or change in the surface topology of MoSe₂ films on the substrate and formation of wrinkles or ripples, which may affect the frequency of the modes. Similar anomalies are also observed in the case of other MX_2 systems [44,46]. To confirm the slippage and/or realignment of MoSe₂ films, we did AFM characterizations after the temperature-dependent Raman measurements of the same flake, as optically shown in Fig. S2(a) in the Supplemental Material [21]. Figure S2(i) in the Supplemental Material [21] shows the AFM image, and the insets depict the step height profile. The step height profile along the white line shows the height of 1L MoSe₂ from the substrate. The average thickness of 1L (F1 region) from the substrate is observed to be \sim 3 nm, which is larger than that of the actual thickness of 1L MoSe₂ from the substrate, reflecting the slippage or realignment of MoSe₂. The step height profile along the blue line shows the height of the 2L along with 1L MoSe₂ from the substrate. The average thickness of 2L from the substrate is \sim 2 nm, reflecting a weak deviation from the reported thickness for the 2L MoSe₂ from the substrate, suggesting the weak effect of induced strain due to TEC mismatch between 2L and substrate. It is in line with the fact that induced strain due to TEC mismatch gradually decreases with the increasing number of layers and becomes negligible for the bulk. To reconfirm this anomalous increase in the 1L height after temperature run, we did AFM measurements on another set of flakes (both 1L and 2L of those shown in Fig. S3 in the Supplemental Material [21]) after temperature run and found 1L and 2L thicknesses of \sim 2.4 and \sim 1 nm from substrate and 1L, respectively, which are in qualitative agreement with measurements on flakes, as shown in Fig. S2(i) in

the Supplemental Material [21]. We note that this increase in AFM height for 1L after temperature run is slightly different at two different spots and may affect the overall results, see Figs. S2(i), S3(e), and S3(f) in the Supplemental Material [21]; this may be due to different magnitude of interaction of the 1L with the substrate at different spots. For 2L, we observed a decrease in the mode frequency, see Figs. 2(b) and 3(b), $< \sim 80$ K. We note that the negative TEC for MoSe₂ in the low-temperature regime (< 30 K) has been estimated theoretically [38], which may give rise to tensile stress < 30 K on lowering the temperature, resulting in the mode frequency softening < 30 K. However, we do observe a decrease in the mode frequencies $< \sim 80$ K, suggesting that MoSe₂ may have a negative TEC even > 30 K and may result in an anomalous decrease in the mode frequency < 80 K.

C. Electron-phonon coupling and lifetimes of the first-order optical modes

Strong electron-phonon coupling, which limits the electronic mobility of semiconductors, can significantly affect the self-energy parameters of the phonon modes, and this may be captured through a detailed temperature-dependent Raman measurement. The temperature-dependent mobility in MoSe₂ was attributed to the scattering of carriers by optical phonons, which corresponds to the fluctuations of the layer thickness [47], implying that the A_{1g} phonon mode with atomic displacements along the c axis and E_{2g}^2 phonon mode with interlayer shear mode may be involved in controlling the mobility of the carriers. In this section, we focus our attention on the temperature dependence of the FWHM of the phonon modes and the role of electron-phonon coupling. In a high-quality sample, FWHM of the phonon modes at finite temperature may be affected by the contributions of two factors: (i) phonon-phonon coupling ($\gamma_{\text{ph-ph}}$) and (ii) electron-phonon interactions ($\gamma_{\text{e-ph}}$). Therefore, the temperature dependence of the FWHM of the phonon modes may be given as [48,49]

$$\gamma(T) = \gamma_{\text{ph-ph}}(T) + \gamma_{\text{e-ph}}(T). \quad (4)$$

The first term $\gamma_{\text{ph-ph}}(T)$ arises from phonon-phonon interactions. Contributions of the three-phonon anharmonic effect to the FWHM of phonons as suggested by Klemens [34] is given as $\gamma_{\text{ph-ph}}(T) = \gamma_{\text{ph-ph}}(0) + C(1 + \frac{2}{e^x - 1})$, where $x = \hbar\omega/2k_B T$, C is a constant parameter, and $\gamma_{\text{ph-ph}}(0)$ is the FWHM at 0 K, and $\gamma_{\text{ph-ph}}(T)$ is expected to dominate at high temperature. The second term $\gamma_{\text{e-ph}}(T)$ arises because of contributions from the electron-phonon interactions. Contribution from electron-phonon interactions to the FWHM may be given as [48,49] $\gamma_{\text{e-ph}}(T) = \gamma_{\text{e-ph}}(0)[(\frac{1}{e^{-x}+1}) - (\frac{1}{e^x+1})]$, where $x = \hbar\omega/2k_B T$, and $\gamma_{\text{e-ph}}(0)$ is the FWHM resulting from the electron-phonon coupling effect at 0 K, and the term $\gamma_{\text{e-ph}}(T)$ is expected to dominate at low temperature. The expression, $\gamma_{\text{e-ph}}(T)$ represents the difference in occupations of states below and above the Fermi energy level and may be used to understand the temperature-dependent shift in the FWHM of the phonon modes. Occupations of the filled states below the Fermi level decrease with increase in temperature, while empty states above the Fermi level are occupied more and may result in narrowing (broadening) of the FWHM with

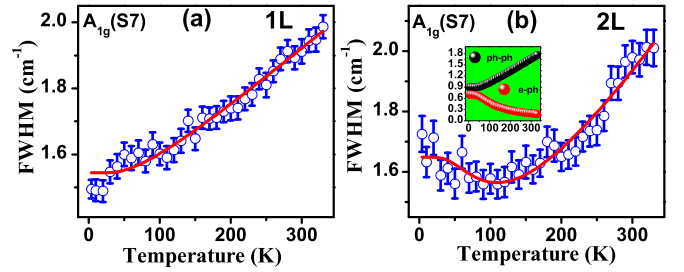


FIG. 4. Temperature-dependent full width at half maximum (FWHM) of the A_{1g} mode for (a) the monolayer (1L) and (b) the bilayer (2L). Solid red lines are the fitted curves described in the text. Inset black and red plots in (b) describe individual contributions to the linewidth from phonon-phonon and electron-phonon coupling, respectively.

increasing (decreasing) temperature [48]. Here, renormalization of the phonon modes may be understood via invoking phonon-induced electron-hole pair creations. With increasing temperature, empty states above the Fermi level start filling up, and this blocks the generation of the phonon-induced electron-hole pairs and hence affects the phonon self-energy. It is expected that, at low (high) temperature, the phonon lifetime will be less (more), and as a result, linewidth will be more (less); based on the pure electron-phonon coupling effect, one expects that linewidth will be more at low temperature and less at a higher temperature. Also, the bandgap in 1L MoSe₂ is significantly higher than in the 2L; therefore, the effect of electron-phonon coupling is expected to be more visible in 2L owing to the reduced bandgap.

Figure 3(c) shows the temperature dependence of the FWHM of the E_{1g} mode for 1L MoSe₂ showing normal temperature dependence, i.e., decreasing with lowering temperature, which may be understood within the phonon-phonon anharmonic interaction picture. Figure 3(d) shows FWHM of the E_{2g}^2 , E_{1g} , and A_{2u}^2 modes for 2L. The FWHM of the E_{2g}^2 mode shows normal temperature dependence from room temperature to ~ 120 K; quite surprisingly, on further lowering of the temperature, it starts to increase until 4 K, attributed to the strong electron-phonon coupling. We note that similar behavior is also observed for the shear modes in graphene [49]. The FWHM of the E_{1g} mode shows normal temperature dependence until ~ 100 K, and it increases slightly < 100 K. On the other hand, the FWHM of the A_{2u}^2 mode shows normal temperature dependence in the entire temperature range. Figures 4(a) and 4(b) show the temperature dependence of the FWHM of the A_{1g} mode for 1L and 2L MoSe₂, respectively. For 1L, the FWHM of the A_{1g} mode shows normal temperature dependence. For 2L, the FWHM of the A_{1g} mode shows normal temperature dependence from 330 to ~ 100 K; interestingly, < 100 K, an increase in FWHM is observed down to 4 K. The FWHM of the modes as a function of temperature are fitted using the above Eq. (4); the solid red lines in Figs. 3(c), 3(d), 4(a), and 4(b) are the fitted curves, and it is in very good agreement with our experimental data. In the 1L, fitting parameters $\gamma_{\text{ph-ph}}(0)$ and $\gamma_{\text{e-ph}}(0)$ of the A_{1g} mode are 1.4 and 0.02 cm^{-1} , respectively, suggesting that the dominating factor is the phonon-phonon anharmonic effect. However, in the case of 2L, $\gamma_{\text{ph-ph}}(0)$ and $\gamma_{\text{e-ph}}(0)$ of the

TABLE III. List of the fitting parameters obtained from FWHM of the first-order optical phonon modes for 1L and 2L MoSe₂. Units are in cm⁻¹.

Modes	Electron-phonon + phonon-phonon coupling model					
	1L			2L		
	C	$\gamma_{\text{ph-ph}}(0)$	$\gamma_{\text{e-ph}}(0)$	C	$\gamma_{\text{ph-ph}}(0)$	$\gamma_{\text{e-ph}}(0)$
$E_{2g}^2(\Gamma)$	–	–	–	0.007 ± 0.001	1.1 ± 0.04	1.3 ± 0.3
$E_{1g}(\Gamma)$	1.1 ± 0.3	3.5 ± 1.5	0.06 ± 1.5	0.9 ± 0.2	2.8 ± 0.9	1.0 ± 0.9
$A_{1g}(\Gamma)$	0.2 ± 0.1	1.4 ± 0.02	0.02 ± 0.01	0.3 ± 0.02	0.6 ± 0.1	0.7 ± 0.08
$E_{2g}^1(\Gamma)$	–	–	–	–	–	–
$A_{2u}^2(\Gamma)$	–	–	–	0.5 ± 0.3	1.9 ± 0.8	0.1 ± 0.6

A_{1g} mode obtained from the fitting are 0.6 and 0.7 cm⁻¹, respectively, suggesting a significant role of electron-phonon coupling at low temperature. It may also explain the observed increase in the FWHM with decreasing temperature <100 K. Overall, $\gamma_{\text{e-ph}}$ is substantial in comparison with $\gamma_{\text{ph-ph}}$ for the 2L system, as anticipated earlier. The fitting parameters obtained from the FWHM for other first-order optical phonon modes are summarized in Table III. Our observation of an anomalous increase in FWHM at low temperature, especially in the 2L, deviating from normal temperature behavior may be understood by keeping the finite role of electron-phonon coupling in these systems.

III. CONCLUSIONS

In conclusion, we performed a comprehensive temperature and polarization-dependent Raman study on CVD-grown MoSe₂ supported by SiO₂ (~300 nm)/Si in a wide temperature and broad spectral range of 10–700 cm⁻¹. Many phonon

modes were observed, up to the fourth order as well as forbidden Raman and IR modes, understood by considering the resonance effect, Fröhlich mechanism of exciton-phonon coupling, and cascade theory of inelastic light scattering. The TEC is extracted for both 1L and 2L MoSe₂ as a function of temperature, and the effect of induced strain from the underlying substrate is found to be significant for the case of a 1L. The observed temperature evolution of the linewidth of the A_{1g} and E_{2g}^2 modes suggests that electron-phonon processes are involved in addition to the phonon-phonon anharmonicity and is found to be dominating in the case of 2L.

ACKNOWLEDGMENTS

PK acknowledges the Department of Science and Technology and IIT Mandi, India, for the financial support. The authors at Mandi acknowledge IIT Mandi for providing the experimental facilities.

-
- [1] T. Sekine, T. Nakashizu, K. Toyoda, K. Uchinokura, and E. Matsuura, *Solid State Commu.* **35**, 371 (1980).
- [2] T. Sekine, M. Izumi, T. Nakashizu, K. Uchinokura, and E. Matsuura, *J. Phys. Soc. Jpn.* **49**, 1069 (1980).
- [3] K. S. Novoselov, A. K. Geim, S. V. Morozov, D. Jiang, Y. Zhang, S. V. Dubonos, I. V. Grigorieva, and A. A. Firsov, *Science* **306**, 666 (2004).
- [4] X. Wang, Y. Gong, G. Shi, W. L. Chow, K. Keyshar, G. Ye, R. Vajtai, J. Lou, Z. Liu, E. Ringe, B. K. Tay, and P. M. Ajayan, *ACS Nano* **8**, 5125 (2014).
- [5] A. A. Puzos, L. Liang, X. Li, K. Xiao, K. Wang, M. M. Samani, L. Basile, J. C. Idrobo, B. G. Sumpter, V. Meunier, and D. B. Geohegan, *ACS Nano* **9**, 6333 (2015).
- [6] S. Larentis, B. Fallahzad, and E. Tutuc, *App. Phys. Lett.* **101**, 223104 (2012).
- [7] H. Li, Q. Zhang, C. C. R. Yap, B. K. Tay, T. H. T. Edwin, A. Olivier, and D. Baillargeat, *Adv. Funct. Mater.* **22**, 1385 (2012).
- [8] A. Splendiani, L. Sun, Y. Zhang, T. Li, J. Kim, C.-Y. Chim, G. Galli, and F. Wang, *Nano Lett.* **10**, 1271 (2010).
- [9] J. Isberg, M. Gabrysch, J. Hammersberg, S. Majdi, K. K. Kovi, and D. J. Twitchen, *Nat. Materials* **12**, 760 (2013).
- [10] N. Kumar, J. He, D. He, Y. Wang, and H. Zhao, *Nanoscale* **6**, 12690 (2014).
- [11] S. Tongay, J. Zhou, C. Ataca, K. Lo, T. S. Matthews, J. Li, J. C. Grossman, and J. Wu, *Nano Lett.* **12**, 5576 (2012).
- [12] M. Yagmurcukardes, C. Bacaksiz, E. Unsal, B. Akbali, R. T. Senger, and H. Sahin, *Phys. Rev. B* **97**, 115427 (2018).
- [13] E. Blundo, M. Felici, T. Yildirim, G. Pettinari, D. Tedeschi, A. Miriametro, B. Liu, W. Ma, Y. Lu, and A. Polimeni, *Phys. Rev. Research* **2**, 012024 (2020).
- [14] D. Yoon, Y.-W. Son, and H. Cheong, *Nano Lett.* **11**, 3227 (2011).
- [15] S. Linas, Y. Magnin, B. Poinso, O. Boisson, G. D. Förster, V. Martinez, R. Fulcrand, F. Tournus, V. Dupuis, F. Rabilloud, L. Bardotti, Z. Han, D. Kalita, V. Bouchiat, and F. Calvo, *Phys. Rev. B* **91**, 075426 (2015).
- [16] R. Yan, J. R. Simpson, S. Bertolazzi, J. Brivio, M. Watson, X. Wu, A. Kis, T. Luo, A. R. H. Walker, and H. G. Xing, *ACS Nano* **8**, 986 (2014).
- [17] P. Kumar, A. Bera, D. V. S. Muthu, P. M. Shirage, A. Iyo, and A. K. Sood, *App. Phys. Lett.* **100**, 222602 (2012).

- [18] P. Kumar, D. V. S. Muthu, L. Harnagea, S. Wurmehl, B. Büchner, and A. K. Sood, *J. Phys.: Condens. Matter* **26**, 305403 (2014).
- [19] I. Bilgin, A. S. Raeliarijaona, M. C. Lucking, S. C. Hodge, A. D. Mohite, A. de L. Bugallo, H. Terrones, and S. Kar, *ACS Nano* **12**, 740 (2018).
- [20] B. Singh, G. A. Cansever, T. Dey, A. Maljuk, S. Wurmehl, B. Büchner, and P. Kumar, *J. Phys.: Condens. Matter* **31**, 065603 (2019).
- [21] See Supplemental Material at <http://link.aps.org/supplemental/10.1103/PhysRevB.105.085419> for details about the sample preparation and measurements as well as temperature dependence of the frequencies and linewidths of second- and higher-order phonon modes. It also includes the details about the origin of second- and higher-order phonon mode as well as the temperature-dependent intensities of the phonon modes.
- [22] P. Tonndorf, R. Schmidt, P. Böttger, X. Zhang, J. Börner, A. Liebig, M. Albrecht, C. Kloc, O. Gordan, D. R. T. Zahn, S. M. de Vasconcellos, and R. Bratschitsch, *Opt. Exp.* **21**, 4908 (2013).
- [23] K. Kim, J.-U. Lee, D. Nam, and H. Cheong, *ACS Nano* **10**, 8113 (2016).
- [24] P. Soubelet, A. E. Bruchhausen, A. Fainstein, K. Nogajewski, and C. Faugeras, *Phys. Rev. B* **93**, 155407 (2016).
- [25] D. Nam, J.-U. Lee, and H. Cheong, *Sci. Rep.* **5**, 17113 (2015).
- [26] X. Lu, M. I. B. Utama, J. Lin, X. Luo, Y. Zhao, J. Zhang, S. T. Pantelides, W. Zhou, S. Y. Quek, and Q. Xiong, *Adv. Mater.* **27**, 4502 (2015).
- [27] D. Kumar, B. Singh, R. Kumar, M. Kumar, and P. Kumar, *Nanotechnology* **32**, 285705 (2021).
- [28] R. M. Martin and T. C. Damen, *Phys. Rev. Lett.* **26**, 86 (1971).
- [29] R. M. Martin and C. M. Varma, *Phys. Rev. Lett.* **26**, 1241 (1971).
- [30] B. Singh, M. Vogl, S. Wurmehl, S. Aswartham, B. Büchner, and P. Kumar, *Phys. Rev. Research* **2**, 023162 (2020).
- [31] D. Kumar, B. Singh, R. Kumar, M. Kumar, and P. Kumar, *J. Phys.: Condens. Matter* **32**, 415702 (2020).
- [32] *Light Scattering in Solid II*, edited by M. Cardona and G. Guntherodt (Springer Verlag, Berlin, 1982).
- [33] R. Loudon, *Adv. Phys.* **50**, 813 (2001).
- [34] P. G. Klemens, *Phys. Rev.* **148**, 845 (1966).
- [35] J. Menendez and M. Cardona, *Phys. Rev. B* **29**, 2051 (1984).
- [36] S. H. El-Mahalaway and B. L. Evans, *Appl. Cryst.* **9**, 403 (1976).
- [37] Y. Ding and B. Xiao, *RSC Adv.* **5**, 18391 (2015).
- [38] C. Sevik, *Phys. Rev. B* **89**, 035422 (2014).
- [39] *Standard Reference Material 739 Certificate* (National Institute of Standards and Technology, 1991).
- [40] E. Blundo, E. Cappelluti, M. Felici, G. Pettinari, and A. Polimeni, *App. Phys. Rev.* **8**, 021318 (2021).
- [41] M. Yang, X. Cheng, Y. Li, Y. Ren, M. Liu, and Z. Qi, *App. Phys. Lett.* **110**, 093108 (2017).
- [42] X. Hu, P. Yasaei, J. Jokisaari, S. Ögüt, A. S.-Khojin, and R. F. Klie, *Phys. Rev. Lett.* **120**, 055902 (2018).
- [43] X. Huang, Y. Gao, T. Yang, W. Ren, H.-M. Cheng, and T. Lai, *Sci. Rep.* **6**, 32236 (2016).
- [44] L. Su, Y. Zhang, Y. Yu, and L. Cao, *Nanoscale* **6**, 4920 (2014).
- [45] C. K. Gan and Y. Y. F. Liu, *Phys. Rev. B* **94**, 134303 (2016).
- [46] D. Kumar, B. Singh, P. Kumar, V. Balakrishnan, and P. Kumar, *J. Phys.: Condens. Matter* **31**, 505403 (2019).
- [47] R. Fivaz and E. Mooser, *Phys. Rev.* **163**, 743 (1967).
- [48] N. Bonini, M. Lazzeri, N. Marzari, and F. Mauri, *Phys. Rev. Lett.* **99**, 176802 (2007).
- [49] C. Cong and T. Yu, *Nat. Commun.* **5**, 4709 (2014).